

Incremental Nonlinear Fault-Tolerant Control of a Quadrotor with Complete Loss of Two Opposing Rotors

Sihao Sun, Xuerui Wang, Qiping Chu, and Coen de Visser

Abstract—In order to further expand the flight envelope of quadrotors under actuator failures, we design a nonlinear sensor-based fault-tolerant controller to stabilize a quadrotor with failure of two opposing rotors in the high-speed flight condition ($> 8\text{m/s}$). The incremental nonlinear dynamic inversion (INDI) approach which excels in handling model uncertainties is adopted to compensate for the significant unknown aerodynamic effects. The internal dynamics of such an underactuated system have been analyzed, and subsequently stabilized by re-defining the control output. The proposed method can be generalized to control a quadrotor under single-rotor-failure and nominal conditions. For validation, flight tests have been carried out in a large-scale open jet wind tunnel. The position of a damaged quadrotor can be controlled in the presence of significant wind disturbances. A linear quadratic regulator (LQR) approach from the literature has been compared to demonstrate the advantages of the proposed nonlinear method in the windy and high-speed flight condition.

I. INTRODUCTION

Multi-rotor drones have demonstrated their ability in a large variety of applications such as surveillance, delivery, and recreation. Due to the potential growth of the drone market in the coming decades, safety issues are of critical concern. Apart from sensor redundancies, and improving operational regulations, fault-tolerant control (FTC) is a key to improving safety in the face of unexpected structural and actuator failures.

Among different types of multi-rotor drones, quadrotors excel in their structural simplicity. However, they suffer more from actuator damages due to a lack of actuator redundancy. Partial damage on the rotors could result in the reduction of control effectiveness, which has been extensively studied in the literature (e.g., [1], [2], [3], [4]). A more challenging problem is the complete loss of one or more rotors. Various control methodologies addressing this problem have been proposed and validated in simulations (e.g., [5], [6], [7], [8], [9], [10]).

In-flight validations have been achieved by several pieces of research where linear control methods were mostly adopted, such as linear quadratic regulator (LQR) [11], proportional-integral-derivative (PID) control [12] and linear parameter varying (LPV) control [13]. The relaxed hovering solution proposed by [14] indicates that the hovering flight of a quadrotor is possible with a loss of up to three rotors. With a specially designed configuration, a vehicle with only a single rotor is tested using LQR with actuator saturations taken into account [15].

The aforementioned literature assumes that the drone is operated around the hovering condition and only limited aerodynamic effects are considered such as the rotational damping [13], [14]. However, in out-door applications, significant aerodynamic forces/moments on the quadrotor are present due to fast cruising speed and large wind disturbances [16], [17]. The system nonlinearity also becomes more significant due to the complex variation of rotor aerodynamic characteristics in high-speed conditions. Therefore, designing a high-speed capable robust nonlinear controller is essential for expanding the flight envelope of a quadrotor subjected to rotor failures, and increasing its robustness against wind disturbances.

Incremental nonlinear dynamic inversion (INDI) is a sensor-based nonlinear control approach that makes use of sensor measurements to reduce its model dependency, thereby improving its robustness against model uncertainties. This approach has been adopted by the aviation industry in several applications, such as the control of fixed-wing aircraft [18], spacecrafts [19], helicopters [20] and multi-rotor drones [21], [22], [23]. In [24], we made use of the INDI controller to control a quadrotor with a single rotor failure in the wind tunnel. The control method has shown its advantage in providing robustness to large aerodynamic disturbances while simplifying gain tuning, and eliminating the need to calculate an equilibrium for linear control design.

However, the INDI controller relies on a dynamic inversion step. This step requires the number of inputs to be no less than the number of outputs. For a quadrotor with only two opposing rotors remain, the attitude control problem becomes under-actuated where the direct inversion is inapplicable. For this reason, we need to redesign the original control outputs of a quadrotor such as the thrust and attitudes. This subsequently results in several internal dynamics of which the stability needs to be guaranteed. The selection of the outputs ensuring stable internal dynamics has been addressed on some under-actuated control problems, e.g., wheeled mobile robots [25], quadrotor position control [26], and the attitude control of space aircraft [27].

The main theoretical contributions of this research are twofold: (1) A detailed analysis of the internal dynamics of quadrotors with complete loss of two opposing rotors; (2) A subsequent novel robust fault-tolerant control method implementing the INDI approach. The controlled quadrotor thereby suffers less from model uncertainties caused by significant aerodynamic effects during high-speed flight.

To validate the proposed controller, flight tests of a quadrotor with failure of two opposing rotors have been performed in an open jet wind tunnel. With limited information on the model, the controller is able to stabilize the damaged quadrotor in wind of over 8 m/s, which is more than half of its nominal

The authors are with Control and Simulation Section, Faculty of Aerospace Engineering, Delft University of Technology, 2629 HS Delft, The Netherlands s.sun-4@tudelft.nl; x.wang-6@tudelft.nl; q.p.chu@tudelft.nl; c.c.devissier@tudelft.nl

maximum flight speed. This could significantly increase the safety of quadrotors by expanding the flight envelope under actuator failure conditions. With slight adaptation, the same control scheme can be used on a quadrotor with a single rotor failure for which the internal dynamics are proved to be inherently stable. A benchmark approach (LQR) has been compared to demonstrate the advantage of the proposed controller in the high-speed and windy flight conditions.

This paper is organized as follows. Sec. II provides information on the quadrotor model and the reduced attitude control. Sec. III introduces the INDI controller and Sec. IV directly provides the detailed controller design for a quadrotor with failure of two opposing rotors. Sec. V elaborates on the selection of control outputs and the stability of internal dynamics. Sec. VI generalizes the proposed method to the single-rotor-failure and the nominal conditions. Finally, Sec. VII and Sec. VIII demonstrate the flight test results in low-speed and high-speed flight conditions respectively.

II. PROBLEM FORMULATION

A. Quadrotor Kinematic and Dynamic Model

There are two coordinate systems considered in this research. The inertial frame $\mathcal{F}_I = \{O_I, \mathbf{x}_I, \mathbf{y}_I, \mathbf{z}_I\}$, is fixed to the ground, with \mathbf{x}_I , \mathbf{y}_I and \mathbf{z}_I pointing to the north, east and aligning with the local gravity. The body frame $\mathcal{F}_B = \{O_B, \mathbf{x}_B, \mathbf{y}_B, \mathbf{z}_B\}$ is fixed to the vehicle, with the origin located at the center of mass; \mathbf{x}_B , \mathbf{y}_B and \mathbf{z}_B point forwards, rightwards and downwards respectively (see Fig. 1). In the following context, the superscript $[\cdot]^I$ and $[\cdot]^B$ indicate the coordinate system in which a vector is expressed.

The equations of motion of a quadrotor are formulated as follows:

$$\dot{\mathbf{P}}^I = \mathbf{V}^I \quad (1)$$

$$m_v \dot{\mathbf{V}}^I = m_v \mathbf{g}^I + \mathbf{R} \mathbf{F}^B \quad (2)$$

$$\dot{\mathbf{R}} = \mathbf{R} \boldsymbol{\Omega}_\times^B \quad (3)$$

$$\mathbf{I}_v \dot{\boldsymbol{\Omega}}^B = -\boldsymbol{\Omega}_\times^B \mathbf{I}_v \boldsymbol{\Omega}^B + \mathbf{M}^B \quad (4)$$

where $\mathbf{P}^I = [X, Y, Z]^T$ and $\mathbf{V}^I = [V_x, V_y, V_z]^T$ represent the position and the velocity of the center of mass in \mathcal{F}_I ; m_v is the vehicle gross mass and \mathbf{I}_v denotes the inertia matrix of the vehicle including rotors. \mathbf{g} is the local gravity vector. $\mathbf{R} \in \text{SO}(3)$ indicates the rotational matrix from \mathcal{F}_B to \mathcal{F}_I . The angular velocity is expressed as $\boldsymbol{\Omega}^B = [p \ q \ r]^T$ where p , q and r denote pitch rate, roll rate and yaw rate respectively. $\boldsymbol{\Omega}_\times$ is the skew symmetric matrix such that $\boldsymbol{\Omega}_\times \mathbf{a} = \boldsymbol{\Omega} \times \mathbf{a}$ for any vector $\mathbf{a} \in \mathbb{R}^3$.

The variables \mathbf{F}^B and \mathbf{M}^B denote the resultant force and moment on the center of mass respectively, projected on \mathcal{F}_B . For a quadrotor with thrust parallel to the \mathbf{z}_B axis and rotor directions shown in Fig. 1, we have

$$\mathbf{F}^B = \begin{bmatrix} 0 \\ 0 \\ -\bar{\kappa} \sum_{i=1}^4 \omega_i^2 \end{bmatrix} + \mathbf{F}_a \quad (5)$$

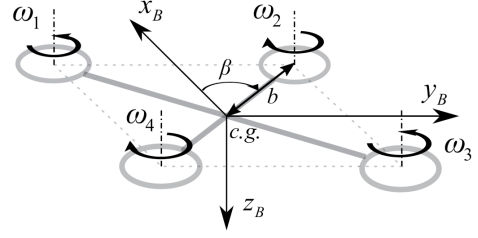


Fig. 1: Definition of geometry parameters, rotor index and directions, and the body frame \mathcal{F}_B .

$$\mathbf{M}^B = \bar{\kappa} \begin{bmatrix} b \sin \beta & -b \sin \beta & -b \sin \beta & b \sin \beta \\ b \cos \beta & b \cos \beta & -b \cos \beta & -b \cos \beta \\ \sigma & -\sigma & \sigma & -\sigma \end{bmatrix} \begin{bmatrix} \omega_1^2 \\ \omega_2^2 \\ \omega_3^2 \\ \omega_4^2 \end{bmatrix} + \begin{bmatrix} I_p q (\omega_1 - \omega_2 + \omega_3 - \omega_4) \\ -I_p p (\omega_1 - \omega_2 + \omega_3 - \omega_4) \\ I_p (\dot{\omega}_1 - \dot{\omega}_2 + \dot{\omega}_3 - \dot{\omega}_4) \end{bmatrix} + \begin{bmatrix} 0 \\ 0 \\ -\gamma r \end{bmatrix} + \mathbf{M}_a \quad (6)$$

where $\bar{\kappa}$ is a thrust coefficient valid in the hovering condition; σ is a constant ratio between the thrust coefficient and drag coefficient of the rotor; b and β are geometry parameters as Fig. 1 shows. Note that $\beta \in (0, \pi/2)$ for a quadrotor. $\omega_i^B = [0, 0, \omega_i]$ is the angular speed of the i th rotor with respect to the body. I_p denotes the moment of inertia of each rotor about the rotational axis. Note that this model assumes that $\|\boldsymbol{\Omega}\| \ll \|\omega_i\|$, thus the magnitude of rotor angular speed with respect to the air is approximated by ω_i . Symbol $\|\cdot\|$ is defined as the L^2 norm of a vector. γ in (6) indicates the aerodynamic yaw damping coefficient [11], [13].

In the high-speed flight condition, there are significant aerodynamic effects such as thrust variation [28], rotor in-plane force [29], rotor moment and airframe aerodynamic [30]. These additional aerodynamic related forces and moments are then expressed as \mathbf{F}_a and \mathbf{M}_a in (5) and (6). They are regarded as model uncertainties that need to be compensated for by the robustness of the control method.

B. Reduced Attitude Control

The concept of reduced attitude control [31] has been adopted by [14] in the quadrotor fault tolerant control problem. We hereby briefly introduce the concept.

For a quadrotor with complete rotor failures, the full state equilibrium becomes unattainable. This is due to the incapacity of the remaining rotors to generate zero yaw moment while producing necessary thrust. As a consequence, the vehicle spins around the yaw axis. And the attitude control is reduced to a thrust vector pointing problem without considering the yaw angle.

Define a unit vector \mathbf{n} fixed to \mathcal{F}_B where $\mathbf{n}^B = [n_x^B, n_y^B, n_z^B]^T$. For a quadrotor with double rotor failures, choosing $\mathbf{n}^B = [0, 0, -1]^T$ is most energy-efficient [11] where \mathbf{n} aligns with the instantaneous thrust direction. Define another unit vector \mathbf{n}_d as the reference of \mathbf{n} , which is calculated by the position controller or manually given by remote control. Then aligning \mathbf{n}_d with \mathbf{n} (or vice versa) becomes the primary task of

the attitude controller. Therefore, we introduce the following relaxed attitude kinematic equation:

$$\dot{\mathbf{n}}_d^B = -\boldsymbol{\Omega}_x \mathbf{n}_d^B + \mathbf{R}^T \dot{\mathbf{n}}_d^I \quad (7)$$

With the expressions $\mathbf{n}_d^B = [h_1, h_2, h_3]^T$ and $\mathbf{R}^T \dot{\mathbf{n}}_d^I = [\lambda_1, \lambda_2, \lambda_3]^T$, the expanded formula of (7) can be given as:

$$\begin{bmatrix} \dot{h}_1 \\ \dot{h}_2 \\ \dot{h}_3 \end{bmatrix} = \begin{bmatrix} 0 & r & -q \\ -r & 0 & p \\ q & -p & 0 \end{bmatrix} \begin{bmatrix} h_1 \\ h_2 \\ h_3 \end{bmatrix} + \begin{bmatrix} \lambda_1 \\ \lambda_2 \\ \lambda_3 \end{bmatrix} \quad (8)$$

The alignment of \mathbf{n} and \mathbf{n}_d thus can be achieved by controlling h_1 and h_2 to track n_x^B and n_y^B respectively. To be specific, with the selection of $\mathbf{n}^B = [0, 0, -1]^T$, h_1 and h_2 need to be stabilized to zero. The other selections of \mathbf{n}^B may be considered for the case with single rotor failure, which has been discussed in [11], [14].

The challenge of the problem is conducting relaxed attitude control of a quadrotor with only two opposing rotors remain in the presence of significant model uncertainties \mathbf{F}_a and \mathbf{M}_a , for instance, in high-speed flight conditions where significant aerodynamic effects become apparent. To achieve this goal, we employ a sensor-based nonlinear control method to be described in Sec. III. The detailed implementation of this method will be provided in Sec. IV.

III. METHODOLOGY

Incremental nonlinear dynamic inversion (INDI) is a sensor-based nonlinear control approach. The approach stems from nonlinear dynamic inversion (NDI) control. INDI reduces the model dependencies of NDI by replacing non-input related model terms with direct sensor measurements, or sensor measurement derived quantities, thereby greatly improving robustness against model uncertainties.

For aircraft systems, including nominal quadrotors, each sub-problem (e.g., the attitude and rate control loops) is fully actuated without internal dynamics to be analyzed [18], [21], [3]. However, for a quadrotor with double rotor failures, the number of control inputs is less than the required output in a conventional cascaded control setup, yielding internal dynamics that have to be stabilized. In the following context, the generalized INDI control considering internal dynamics will be briefly reviewed. Readers may refer to [32] and [33] for further details.

Consider a nonlinear input affine system

$$\begin{aligned} \dot{\mathbf{x}} &= \mathbf{f}(\mathbf{x}) + \mathbf{G}(\mathbf{x})\mathbf{u} \\ \mathbf{y} &= \mathbf{h}(\mathbf{x}) \end{aligned} \quad (9)$$

where $\mathbf{f} : \mathbb{R}^n \rightarrow \mathbb{R}^n$ and $\mathbf{h} : \mathbb{R}^n \rightarrow \mathbb{R}^l$ are smooth vector fields. $\mathbf{G} : \mathbb{R}^n \rightarrow \mathbb{R}^{n \times m}$ is a function mapping with smooth vector fields as columns. The number of outputs is not larger than the number of inputs (i.e., $l \leq m$). There exists a nonlinear transformation $\mathbf{T} : \mathbb{R}^n \rightarrow \mathbb{R}^n$ such that the states \mathbf{x} can be transformed to the normal form including internal states $\boldsymbol{\eta}$ and external states $\boldsymbol{\xi}$:

$$\begin{bmatrix} \boldsymbol{\eta} \\ \boldsymbol{\xi} \end{bmatrix} = \begin{bmatrix} \boldsymbol{\phi}(\mathbf{x}) \\ \boldsymbol{\theta}(\mathbf{x}) \end{bmatrix} = \mathbf{T}(\mathbf{x}) \quad (10)$$

where

$$\boldsymbol{\theta}(\mathbf{x}) = [\boldsymbol{\theta}_1(\mathbf{x}), \boldsymbol{\theta}_2(\mathbf{x}), \dots, \boldsymbol{\theta}_l(\mathbf{x})]^T \quad (11)$$

with

$$\boldsymbol{\theta}_i(\mathbf{x}) = [h_i(\mathbf{x}), L_f h_i(\mathbf{x}), \dots, L_f^{\rho_i-1} h_i(\mathbf{x})], \quad i = 1, 2, \dots, l \quad (12)$$

where $h_i(\mathbf{x})$ indicates the i th element in the vector field \mathbf{h} . The notation $L_f^{\rho_i} h_i(\mathbf{x})$ indicates the ρ_i th order Lie derivative of the function h_i with respect to the vector fields $\mathbf{f}(\mathbf{x})$ [33]. ρ_i indicates the relative degree of the i th output y_i .

By defining $\bar{\rho} = \sum_{i=1}^l \rho_i$ as the sum of relative degrees of each output, one can define the transformation $\boldsymbol{\phi}(\mathbf{x}) = [\phi_1(\mathbf{x}), \phi_2(\mathbf{x}), \dots, \phi_{n-\bar{\rho}}(\mathbf{x})]$. The selection of $\boldsymbol{\phi}(\mathbf{x})$ is not unique, but has to satisfy the following condition:

$$\frac{\partial \phi_i}{\partial \mathbf{x}} \mathbf{G}(\mathbf{x}) = 0, \quad i = 1, 2, \dots, n - \bar{\rho} \quad (13)$$

namely the first-order derivative of $\boldsymbol{\eta}$ as defined per (10) does not include control input \mathbf{u} . The nonlinear transformation $\mathbf{T}(\mathbf{x})$ is a diffeomorphism (i.e., smooth and invertible) in the domain of interest.

As a consequence, the problem is transformed to the normal form

$$\begin{aligned} \dot{\boldsymbol{\eta}} &= \mathbf{f}_{\boldsymbol{\eta}}(\boldsymbol{\eta}, \boldsymbol{\xi}) \\ \dot{\boldsymbol{\xi}} &= \mathbf{A}_c \boldsymbol{\xi} + \mathbf{B}_c [\boldsymbol{\alpha}(\mathbf{x}) + \mathcal{B}(\mathbf{x})\mathbf{u}] \\ \mathbf{y} &= \mathbf{C}_c \boldsymbol{\xi} \end{aligned} \quad (14)$$

where the triplet $(\mathbf{A}_c, \mathbf{B}_c, \mathbf{C}_c)$ is a canonical form representation of l chains of ρ_i integrators ($i = 1, 2, \dots, l$); $\boldsymbol{\alpha} : \mathbb{R}^n \rightarrow \mathbb{R}^l$ and $\mathcal{B} : \mathbb{R}^n \rightarrow \mathbb{R}^{m \times l}$ are mappings determined by the system (9). Subsequently, the output dynamics can be represented as

$$\mathbf{y}^{(\rho)} = \boldsymbol{\alpha}(\mathbf{x}) + \mathcal{B}(\mathbf{x})\mathbf{u} \quad (15)$$

where $\mathbf{y}^{(\rho)} = [y_1^{(\rho_1)}, y_2^{(\rho_2)}, \dots, y_l^{(\rho_l)}]^T$. The NDI control law is designed as

$$\mathbf{u}_{\text{ndi}} = \mathcal{B}(\mathbf{x})^{-1}(\mathbf{v} - \boldsymbol{\alpha}(\mathbf{x})) \quad (16)$$

where $\mathbf{v} \in \mathbb{R}^n$ is called the pseudo-input. With a full knowledge of $\boldsymbol{\alpha}(\mathbf{x})$ and $\mathcal{B}(\mathbf{x})$, control law (16) yields the closed loop dynamics

$$\mathbf{y}^{(\rho)} = \mathbf{v} \quad (17)$$

For a command tracking problem with reference output $\mathbf{y}_{\text{ref}} \in \mathbb{R}^l$ that is ρ th order differentiable, selecting

$$\mathbf{v} = -\mathbf{K}(\boldsymbol{\xi} - \boldsymbol{\xi}_{\text{ref}}) + \mathbf{y}_{\text{ref}}^{(\rho)} \quad (18)$$

ensures that the reference output is being tracked asymptotically, where the gains \mathbf{K} is selected such that $\mathbf{A}_c - \mathbf{B}_c \mathbf{K}$ is Hurwitz. The reference $\boldsymbol{\xi}_{\text{ref}}$ is denoted as

$$\begin{aligned} \boldsymbol{\xi}_{\text{ref}} &= [\boldsymbol{\psi}_1, \boldsymbol{\psi}_2, \dots, \boldsymbol{\psi}_l]^T, \\ \boldsymbol{\psi}_i &= [y_{\text{ref},i}, y_{\text{ref},i}^{(1)}, \dots, y_{\text{ref},i}^{(\rho_i-1)}], \quad i = 1, 2, \dots, l \end{aligned} \quad (19)$$

In reality, the nonlinear model dependent terms $\boldsymbol{\alpha}(\mathbf{x})$ and $\mathcal{B}(\mathbf{x})$ are almost impossible to be obtained due to inevitable model uncertainties. In view of this, we take the first-order Taylor series expansion of (15) around the condition at the

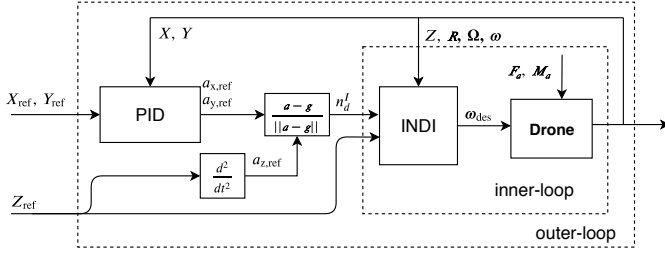


Fig. 2: The two-loops cascaded control scheme using PID as outer-loop position control and INDI as inner-loop altitude / attitude control.

last sensor sampling moment $t - \Delta t$ (denoted by subscript $[\cdot]_0$), then (15) becomes [32]

$$\begin{aligned} \mathbf{y}^{(\rho)} &= \boldsymbol{\alpha}(\mathbf{x}) + \mathcal{B}(\mathbf{x})\mathbf{u} \\ &= \mathbf{y}_0^{(\rho)} + \mathcal{B}(\mathbf{x}_0)\Delta\mathbf{u} + \left. \frac{\partial[\boldsymbol{\alpha}(\mathbf{x}) + \mathcal{B}(\mathbf{x})\mathbf{u}]}{\partial\mathbf{x}} \right|_0 \Delta\mathbf{x} + O(\Delta\mathbf{x}^2) \\ &\triangleq \mathbf{y}_0^{(\rho)} + \mathcal{B}(\mathbf{x}_0)\Delta\mathbf{u} + \boldsymbol{\delta}(\mathbf{x}, \Delta t) \end{aligned} \quad (20)$$

where $\Delta\mathbf{u} = \mathbf{u} - \mathbf{u}_0$, $\Delta\mathbf{x} = \mathbf{x} - \mathbf{x}_0$. Design the incremental nonlinear dynamic inversion (INDI) control as

$$\bar{\mathbf{u}}_{\text{indi}} = \hat{\mathcal{B}}(\mathbf{x}_0)^{-1}(\boldsymbol{\nu} - \mathbf{y}_0^{(\rho)}) + \mathbf{u}_0 \quad (21)$$

where $\boldsymbol{\nu}$ is selected as per (18), while $\hat{\mathcal{B}}$ is the estimated control effectiveness matrix. As a result, the closed-loop tracking error ($\mathbf{e} = \mathbf{y} - \mathbf{y}_{\text{ref}}$) dynamics are $\dot{\mathbf{e}} = (\mathbf{A}_c - \mathbf{B}_c\mathbf{K})\mathbf{e} + \mathbf{B}_c\boldsymbol{\varepsilon}_{\text{indi}}$, where $\boldsymbol{\varepsilon}_{\text{indi}}$ is the residual error caused by model uncertainties. The boundedness of $\boldsymbol{\varepsilon}_{\text{indi}}$ and \mathbf{e} has been proved in [34].

In INDI control, the model information of $\boldsymbol{\alpha}(\mathbf{x})$ is not needed for implementation, which greatly reduces the effort of modeling. The control effectiveness matrix $\hat{\mathcal{B}}$ is relatively easier to be estimated offline or identified online [21]. Apart from its reduced model dependency, INDI control also has enhanced robustness as compared to its classical NDI counterpart [34].

Due to the measurement noise, the variables \mathbf{x}_0 , \mathbf{y}_0 can be low-pass filtered in practice. To synchronize the time delay caused by these filters, \mathbf{u}_0 also need to be filtered with the same cut-off frequency [21]. We use subscript $[\cdot]_f$ to denote the filtered variables (e.g., $\mathbf{x}_0 \rightarrow \mathbf{x}_f$, $\mathbf{y}_0 \rightarrow \mathbf{y}_f$ and $\mathbf{u}_0 \rightarrow \mathbf{u}_f$). Consequently, the INDI control law becomes

$$\mathbf{u}_{\text{indi}} = \hat{\mathcal{B}}(\mathbf{x}_f)^{-1}(\boldsymbol{\nu} - \mathbf{y}_f^{(\rho)}) + \mathbf{u}_f \quad (22)$$

We will elaborate on applying the INDI control law (22) to the quadrotor control problem in the following sections.

IV. CONTROLLER DESIGN

The detailed design process of the controller for a quadrotor with complete failure of two opposing rotors is presented in this section. In general, we use a cascaded controller with two loops (Fig. 2), where INDI is applied in the inner-loop for compensating model uncertainties (\mathbf{M}_a , \mathbf{F}_a).

A. Outer-loop Design

The outer-loop contains a horizontal position controller that computes the acceleration command from the reference horizontal position denoted by X_{ref} and Y_{ref} . Due to the linear property of translational kinematics, a linear method such as a PID controller can be employed. In addition, the reference altitude Z_{ref} needs to be second-order differentiable. Therefore, we have

$$\mathbf{a}_{\text{ref}} = \begin{bmatrix} -k_p e_x - k_d \dot{e}_x - k_i \int e_x dt \\ -k_p e_y - k_d \dot{e}_y - k_i \int e_y dt \\ \ddot{Z}_{\text{ref}} \end{bmatrix} \quad (23)$$

where $e_x = X - X_{\text{ref}}$, $e_y = Y - Y_{\text{ref}}$ denote the horizontal position errors in \mathcal{F}_T ; control gains k_p , k_i and k_d are positive. Then \mathbf{n}_d for reduced attitude control (see Sec. II) can be calculated by

$$\mathbf{n}_d = \frac{\mathbf{a}_{\text{ref}} - \mathbf{g}}{\|\mathbf{a}_{\text{ref}} - \mathbf{g}\|} \quad (24)$$

It is possible to replace (23) by more sophisticated position controllers to obtain \mathbf{a}_{ref} , which will not be elaborated in this research.

B. Inner-loop Design

The altitude control is included in the inner-loop controller since the altitude reference Z_{ref} is related to rotor thrust which contains model uncertainties \mathbf{F}_a . Consequently, the inner-loop is a combination of altitude and attitude control using the INDI approach.

States for the inner-loop control are defined as $\mathbf{x}_{\text{in}} = [h_1, h_2, p, q, r, Z, V_z]^T$. There are two different scenarios for a quadrotor with two opposite rotor failures. If only rotor 1 and 3 remain functional, we define the control input as

$$\mathbf{u} = [u_1, u_2]^T \triangleq [\omega_1^2, \omega_3^2]^T, \quad s_l = 1 \quad (25)$$

If only rotor 2 and 4 remain, then

$$\mathbf{u} = [u_1, u_2]^T \triangleq [\omega_2^2, \omega_4^2]^T, \quad s_l = -1 \quad (26)$$

where $s_l \in \{-1, 1\}$ is a parameter indicating the type of failure.

Since the product of inertia is negligible compared with the moment of inertia for a typical quadrotor, we can assume a diagonal inertia matrix $\mathbf{I}_v = \text{diag}(I_x, I_y, I_z)$. Thus the state equations for the inner-loop states \mathbf{x} can be derived from (4) and (7), yielding

$$\begin{bmatrix} \dot{Z} \\ \dot{V}_z \\ \dot{h}_1 \\ \dot{h}_2 \\ \dot{p} \\ \dot{q} \\ \dot{r} \end{bmatrix} = \begin{bmatrix} V_z \\ g + F_{a,z} - R_{33}\bar{k}(u_1 + u_2)/m_v \\ h_3 p - h_1 r + \lambda_2 \\ -h_3 q + h_2 r + \lambda_1 \\ A_x r q - 2a_x q \bar{\omega} s_n + M_{a,x} + s_l G_p(u_1 - u_2) \\ A_y r p + 2a_y p \bar{\omega} s_n + M_{a,y} + G_q(u_1 - u_2) \\ A_z p q - \gamma r / I_z + M_{a,z} - s_n G_r(u_1 + u_2) \end{bmatrix} \quad (27)$$

where

$$A_x = (I_y - I_z)/I_x, \quad A_y = (I_z - I_x)/I_y, \quad A_z = (I_x - I_y)/I_z \quad (28)$$

$$a_x = I_p/I_x, \quad a_y = I_p/I_y, \quad g = \|\mathbf{g}\| \quad (29)$$

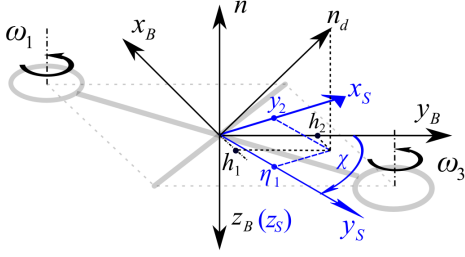


Fig. 3: Definition of \mathcal{F}_S , y_2 , η_1 and χ when rotor 2 and rotor 4 are removed.

where R_{33} in (27) represents the entry at the third row and the third column of the matrix \mathbf{R} ; $\bar{\omega}$ is the average angular rate of the remaining rotors; $s_n \in \{-1, 1\}$ indicates the handedness of the remaining rotors with 1 clockwise and -1 counterclockwise. G_p , G_q and G_r are control effectiveness on angular accelerations, where

$$G_p = \bar{\kappa} \sin \beta / I_x, \quad G_q = \bar{\kappa} \cos \beta / I_y, \quad G_r = \sigma \bar{\kappa} / I_z \quad (30)$$

Normally, $|G_r| \ll \min\{|G_p|, |G_q|\}$. Note that state equations (27) are nonlinear and contain model uncertainties ($F_{a,z}$, $M_{a,x}$, $M_{a,y}$ and $M_{a,z}$). The following content in this section designs the INDI control law (22) for this specific problem.

1) *Control output definition:* Since there are only two inputs remain, we can select a maximum of two variables as control outputs. To guarantee altitude tracking, we choose the first output as

$$y_1 = Z \quad (31)$$

The second output have to be associated with the reduced attitude control. Recall that in Sec. II-B, \mathbf{n} needs to align with \mathbf{n}_d by manipulating the vehicle attitude, and h_1 and h_2 of (8) need to converge to zero. We hereby introduce a new coordinate system $\mathcal{F}_S = \{O_S, \mathbf{x}_S, \mathbf{y}_S, \mathbf{z}_S\}$ that is fixed with respect to the body frame. As Fig. 3 illustrates, \mathcal{F}_S is generated by rotating the body frame about \mathbf{z}_B . The rotation angle is denoted as χ .

The second output y_2 is then defined as the projection of \mathbf{n}_d on \mathbf{x}_S . In other words, y_2 becomes a linear combination of h_1 and h_2 scheduled by the angle χ :

$$y_2 = h_1 \cos \chi + h_2 \sin \chi \quad (32)$$

Meanwhile, the projection of \mathbf{n}_d on \mathbf{y}_S that is perpendicular to the second output y_2 remains uncontrolled (see Fig. 3). We will elaborate in Sec. V that this variable, denoted by η_1 , is one of the internal states to be stabilized by properly selecting the angle χ .

Due to the symmetric property of a quadrotor, we can determine χ by selecting its absolute value, using the following relationship:

$$\chi = s_l |\chi| \quad (33)$$

It is noteworthy that $|\chi|$ is associated with the control performance, which can be analogous to physically informed control gains. The selection of $|\chi|$ will be further discussed in Sec. V.

2) *Control effectiveness estimation:* After defining the outputs we can take second order derivative of both y_1 and y_2 , yielding

$$\begin{aligned} \ddot{y}_1 &= g + F_{a,z} - R_{33} \bar{\kappa} (u_1 + u_2) / m_v \\ &= \alpha_1 + B_1 (u_1 + u_2) \end{aligned} \quad (34)$$

$$\begin{aligned} \ddot{y}_2 &= \ddot{h}_1 \cos \chi + \ddot{h}_2 \sin \chi \\ &= \alpha_2(\mathbf{x}, \chi) + B_2 (u_1 - u_2) \end{aligned} \quad (35)$$

where α_2 can be calculated from (27) whereupon includes nonlinear terms and model uncertainties. B_1 and B_2 are control effectiveness on y_1 and y_2 respectively:

$$B_1 = -\bar{\kappa} R_{33,f} / m_v \quad (36)$$

$$\begin{aligned} B_2 &= s_l h_{3,f} (G_p \sin \chi - G_q \cos \chi) \\ &= -\frac{h_{3,f} \bar{\kappa} b \sin \beta}{I_x \cos \zeta} \sin(\zeta - |\chi|) \end{aligned} \quad (37)$$

where ζ is a positive virtual angle defined as

$$\zeta = \tan^{-1} \left(\frac{I_x}{I_y} \cot \beta \right) \quad (38)$$

Now, from (34) and (35), the estimated control effectiveness matrix in (22) can be described as

$$\hat{\mathbf{B}}(\mathbf{x}_f) = \begin{bmatrix} B_1 & B_1 \\ B_2 & -B_2 \end{bmatrix} \quad (39)$$

The estimation error of $\hat{\mathbf{B}}$ mainly stems from the error of m_v , I_x , I_y , and $\bar{\kappa}$. Note that the filtered variables $R_{33,f}$ and $h_{3,f}$ are used in (36) and (37) because $\hat{\mathbf{B}}$ is a function of \mathbf{x}_f as per (22).

Remark 1: As indicated by (35) and (37), the system has the largest control effectiveness on y_2 when $|\sin(\zeta - |\chi|)| = 1$. On the contrary, the control effectiveness becomes zero when $\sin(\zeta - |\chi|) = 0$. Small control effectiveness leads to large control input command and subsequently deteriorates the control performance with the presence of actuator position and rate limit. Therefore, we enforce the effectiveness on y_2 to be greater than the minimum of G_p and G_q , which yields the following constraint on $|\chi|$:

$$r_B(|\chi|) \triangleq \frac{|B_2(|\chi|)|}{\min\{|G_p|, |G_q|\}} \geq 1 \quad (40)$$

In addition, the following constraints are made to prevent $B_1 = B_2 = 0$, which is rather easy to fulfill:

- $R_{33,f} \neq 0$: the thrust direction does not remain in the horizontal plane of \mathcal{F}_I .
- $h_{3,f} \neq 0$: \mathbf{n}_d is not perpendicular to the current thrust direction ($-\mathbf{z}_B$).

3) *Second derivative of the output:* $\ddot{\mathbf{y}}_f = [\ddot{y}_{1,f}, \ddot{y}_{2,f}]^T$ in (22) can be obtained by directly taking the second-order derivative of filtered outputs. This, however, is prone to be detrimentally affected by measurement noise. Therefore, we can approximated $\ddot{y}_{1,f}$ by:

$$\ddot{y}_{1,f} = \ddot{Z}_f = \dot{V}_{z,f} \simeq a_{z,f} / R_{33,f} \quad (41)$$

where $a_{z,f}$ is the projection of the filtered accelerometer measurement on \mathbf{z}_B .

$\ddot{y}_{2,f}$ can be obtained by numerically differentiating filtered \ddot{y}_2 . The latter can be derived from (8) and (32):

$$\ddot{y}_2 = \cos \chi (-h_3 q + h_2 r + \lambda_1) + \sin \chi (h_3 p - h_1 r + \lambda_2) \quad (42)$$

4) *Pseudo-input definition*: The last step is to define the pseudo-input \mathbf{v} as per (18). As presented in (34) and (35), the control input \mathbf{u} appears after taking the second derivative of both y_1 and y_2 . Thus the system relative degrees are $\rho_1 = \rho_2 = 2$. According to (11) and (12), there are four external states:

$$[\xi_1, \xi_2, \xi_3, \xi_4]^T = [y_1, \dot{y}_1, y_2, \dot{y}_2]^T = \begin{bmatrix} Z \\ V_z \\ h_1 \cos \chi + h_2 \sin \chi \\ (-h_3 q + h_2 r + \lambda_1) \cos \chi + (h_3 p - h_1 r + \lambda_2) \sin \chi \end{bmatrix} \quad (43)$$

For this problem, the output reference is defined as

$$\mathbf{y}_{\text{ref}} = [Z_{\text{ref}}, h_{1,\text{ref}} \cos \chi + h_{2,\text{ref}} \sin \chi]^T = [Z_{\text{ref}}, 0]^T \quad (44)$$

Then, by substituting (43) and (44) into (18), we obtain the pseudo-input

$$\mathbf{v} = \begin{bmatrix} -k_{z,p}(\xi_1 - Z_{\text{ref}}) - k_{z,d}(\xi_2 - \dot{Z}_{\text{ref}}) + \ddot{Z}_{\text{ref}} \\ -k_{a,p}\xi_3 - k_{a,d}\xi_4 \end{bmatrix} \quad (45)$$

with positive gains $k_{z,p}$, $k_{z,d}$, $k_{a,p}$, $k_{a,d}$ to be tuned.

Eventually, the control effectiveness $\hat{\mathbf{B}}$, $\ddot{\mathbf{y}}$ and \mathbf{v} is substituted into (22) to obtain \mathbf{u}_{indi} . The rotor speed command of the remaining rotors can be subsequently calculated using (25) or (26).

V. STABILITY ANALYSIS OF INTERNAL DYNAMICS

For the attitude/altitude inner-loop, internal states that need to be analyzed regarding their stability properties. As (32) shows, the selection of χ is of great importance for influencing the internal dynamics, which will be elaborated in this section.

A. Relaxed Trimming Equilibrium

The relaxed trimming equilibrium is an extension of the relaxed hovering equilibrium [14] to the high-speed flight regime where the aerodynamic drag becomes apparent. Note that the term trimming indicates the condition at a constant forward flight velocity. As Fig. 4a shows, the quadrotor spins about the axis \mathbf{n} which represents the average thrust in a single revolution. In the relaxed trimming equilibrium, this averaged thrust is balanced with the average drag force (denoted by $\mathbf{F}_{a,xy}$) and the gravity. If we assume the constancy of \mathbf{M}_a and $\mathbf{F}_{a,z}$ in (27), we have

$$\mathbf{x}_{\text{in}} = \bar{\mathbf{x}}_{\text{in}} = [\bar{h}_1, \bar{h}_2, \bar{p}, \bar{q}, \bar{r}, \bar{Z}, \bar{V}_z]^T \quad (46)$$

Specifically, if $\mathbf{n}^B = [0, 0, -1]^T$, we have

$$\bar{h}_1 = \bar{h}_2 = \bar{p} = \bar{q} = 0 \quad (47)$$

In practice, \mathbf{M}_a and \mathbf{F}_a are non-stationary. Thus variables h_1 , h_2 , p , q and r normally oscillate about the equilibrium. Nevertheless, as was analysed in [24], the average thrust direction remain unchanged as long as the reduced attitude h_1 and h_2 are bounded. The variation of yaw rate r is also

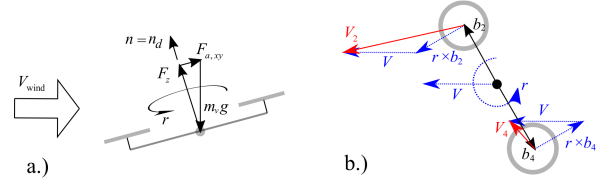


Fig. 4: a.) Illustration of the force equilibrium at the relaxed trimming equilibrium. b.) The local velocities of the remaining rotors are different due to the high angular and translational speed of the drone (rotor 2 and 4 remain).

relatively small compared to \bar{r} . We therefore assume the constancy of r in the following analysis.

Due to the spinning motion around the yaw axis during forward flight, the local airspeed and angle of attack of each rotor can be different (see Fig. 4b). The difference of local airspeed leads to the variation of thrust coefficient κ of each remaining rotor [30]. The rotor speeds, therefore, vary with the heading angle and the variation grows with the flight speed.

B. Internal Dynamics

The internal dynamics are analyzed around the relaxed-trimming equilibrium. The following assumptions are further made to derive the internal states.

Assumption 1: \mathbf{F}_a and \mathbf{M}_a are independent from the control input \mathbf{u} .

Assumption 2: The attitude reference \mathbf{n}_d^I is slowly time-varying, thus $\dot{\mathbf{n}}_d^I = [\lambda_1, \lambda_2, \lambda_3]^T \approx 0$.

Assumption 3: The average rotor speed $\bar{\omega}$ is considered as a constant that is independent from the control input \mathbf{u} .

Note that *Assumption 3* holds because of the near-constancy of the resultant thrust during the trimming condition, which has been verified from the flight data. But this assumption is invalid during aggressive thrust variation, such as vertical maneuvers. Nevertheless, the flight experiments given in Sec. VII will demonstrate that the internal dynamics are still stable during vertical maneuvers.

Since \mathbf{x}_{in} has seven states in total and there are four external states as per (43), we need to determine three internal states. The selection of internal states is not unique as long as the condition (13) is satisfied, namely the first-order derivatives of $\boldsymbol{\eta}$ do not include \mathbf{u} . Based on the above assumptions, we hereby make the following choices for the internal states:

$$\begin{bmatrix} \eta_1 \\ \eta_2 \\ \eta_3 \end{bmatrix} = \begin{bmatrix} -h_1 \sin \chi + h_2 \cos \chi \\ q \cos \zeta - s_l p \sin \zeta \\ r + s_n \mu V_z \end{bmatrix} \quad (48)$$

where

$$\mu = m_v \sigma / h_3 \quad (49)$$

and ζ is defined as per (38). Note that the first internal state η_1 is the projection of \mathbf{n}_d on \mathbf{y}_S axis as illustrated in Fig. 3. Substituting (47) into (48) gives the internal state at relaxed hovering equilibrium $\bar{\boldsymbol{\eta}} = \boldsymbol{\phi}(\bar{\mathbf{x}}_{\text{in}}) = [0, 0, \bar{r} + s_n \mu \bar{V}_z]^T$.

Proposition 1: The internal dynamics of the inner-loop system are locally asymptotically stable at the relaxed trimming equilibrium $\bar{\mathbf{x}}_{\text{in}}$ if and only if $\chi = s_l |\chi|$ is selected such

that every eigenvalue of the following A_1 matrix has strictly negative real part:

$$A_1 = \frac{s_l}{\sin(|\chi| - \zeta)} \begin{bmatrix} -\bar{r} \cos(|\chi| - \zeta) & 1 \\ -\bar{r} \Lambda & \Delta \end{bmatrix} \quad (50)$$

where

$$\Lambda = (A_x \bar{r} - 2a_x \bar{\omega} s_n) \sin^2 \zeta + (A_y \bar{r} + 2a_y \bar{\omega} s_n) \cos^2 \zeta \quad (51)$$

$$\Delta = -(A_x \bar{r} - 2a_x \bar{\omega} s_n) \sin \zeta \sin |\chi| + (A_y \bar{r} + 2a_y \bar{\omega} s_n) \cos \zeta \cos \chi \quad (52)$$

Proof. The transformation $[\eta, \xi]^T = T(x)$ expressed as (43) and (48) is a diffeomorphism if $h_3 \sin(\zeta - |\chi|) \neq 0$. The inverse transformation $x = T^{-1}([\xi, \eta])$ thus can be obtained as

$$\begin{bmatrix} Z \\ V_z \\ h_1 \\ h_2 \\ p \\ q \\ r \end{bmatrix} = \begin{bmatrix} \xi_1 \\ \xi_2 \\ \xi_3 \cos \chi - \eta_1 \sin \chi \\ \xi_3 \sin \chi + \eta_1 \cos \chi \\ \frac{h_3 s_n s_l (\xi_4 \cos \zeta + \eta_2 \cos \chi) + (m_v \sigma \xi_2 - \eta_3 h_3) s_l \eta_1 \cos \zeta}{h_3^2 s_n \sin(|\chi| - \zeta)} \\ \frac{h_3 s_n (\xi_4 \sin \zeta + \eta_2 \sin |\chi|) + (m_v \sigma \xi_2 - \eta_3 h_3) \eta_1 \sin \zeta}{h_3^2 s_n \sin(|\chi| - \zeta)} \\ (\eta h_3 - m_v \sigma \xi_2) / (h_3 s_n) \end{bmatrix} \quad (53)$$

Then the dynamic equation of the internal states is derived as

$$\dot{\eta} = \tilde{f}_\eta(x; \chi) = \tilde{f}_\eta(T^{-1}(\eta, \xi); \chi) = f_\eta(\eta, \xi; \chi) \quad (54)$$

A sufficient condition of the local stability of internal dynamics can be established via the notion of the zero dynamics [27]:

$$\dot{\eta} = f_\eta(\eta, 0; \chi) \quad (55)$$

By substituting (53) into (55), we have:

$$\dot{\eta}_1 = \frac{\eta_2 s_n h_3^2 - \eta_1 \eta_3 \cos(|\chi| - \zeta) h_3}{h_3 s_n s_l \sin(|\chi| - \zeta)} \quad (56)$$

$$\dot{\eta}_2 = \frac{\sin \zeta (-2a_x \bar{\omega} + A_x \eta_3) (\eta_1 \eta_3 \sin \zeta - \eta_2 h_3 s_n \sin |\chi|) - \cos \zeta (2a_y \bar{\omega} + A_y \eta_3) (\eta_1 \eta_3 \cos \zeta - \eta_2 h_3 s_n \cos \chi)}{s_l h_3 \sin(|\chi| - \zeta)} \quad (57)$$

$$\dot{\eta}_3 = -\frac{s_l A_z (\eta_1 \eta_3 \cos \zeta - \eta_2 h_3 s_n \cos \chi) (\eta_1 \eta_3 \sin \zeta - \eta_2 h_3 s_n \sin |\chi|)}{h_3^2 \sin(|\chi| - \zeta)^2} \quad (58)$$

According to the first Lyapunov criterion, the equilibrium of the nonlinear system is asymptotically stable if the linearized system is asymptotically stable [33]. At the relaxed trimming equilibrium, the internal states are $\bar{\eta} = [0, 0, \bar{r} + s_n \mu \bar{V}_z]^T$, and the local linearized system is derived from (56)-(58) as

$$\begin{bmatrix} \dot{\eta}_1 \\ \dot{\eta}_2 \\ \dot{\eta}_3 \end{bmatrix} = \begin{bmatrix} A_1 & \mathbf{0}_{2 \times 1} \\ 0 & -\gamma / I_z \end{bmatrix} \begin{bmatrix} \eta_1 \\ \eta_2 \\ \eta_3 \end{bmatrix} - \bar{\eta} \quad (59)$$

where A_1 is expressed as per (50). Note that the yaw damping γ is positive definite and the system matrix of (59) is block diagonal. Therefore, if A_1 is Hurwitz, namely every eigenvalue of A_1 has strictly negative real part, then the linear system (59) is asymptotically stable. Subsequently the local asymptotic stability of the internal dynamics is satisfied. \square

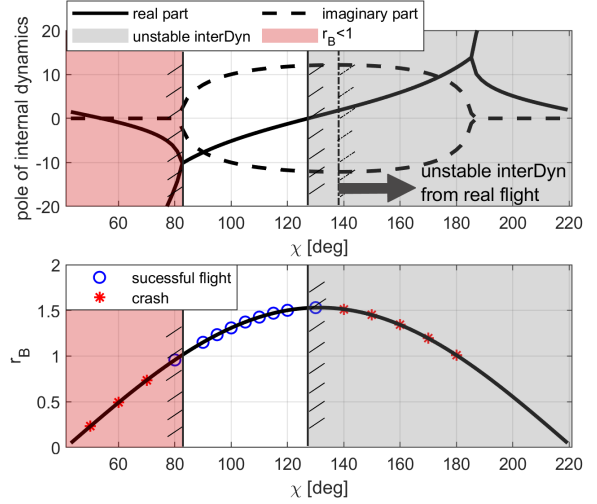


Fig. 5: Poles of matrix A_1 and r_B varying with $|\chi| \in (\zeta, \zeta + \pi)$. The unshaded area is the permitted region of $|\chi|$. Tests in the simulation are marked in the bottom plot with different symbols indicating if the flight succeeds. Unstable internal dynamic region obtained from real flight data in is shown in the top plot, which slightly moves rightward indicating a larger admissible region of $|\chi|$. Though A_1 is stable in the area shaded red, crash still occurs because of $r_B < 1$ that violates the constraint (40).

One may approximate \bar{r} and $\bar{\omega}$ from (27) with M_a and F_a neglected:

$$\bar{r} = -s_n m_v g \sigma / \gamma, \quad \bar{\omega} = \sqrt{\frac{m_v g}{2\bar{k}}} \quad (60)$$

Remark 2: From (50) and (60) we have

$$\text{Re}(\lambda_{A_1}(s_l s_n, |\chi|)) = -\text{Re}(\lambda_{A_1}(-s_l s_n, |\chi|)) \quad (61)$$

where λ_{A_1} denotes eigenvalues of A_1 . Note that for a specific quadrotor, the value of $s_l s_n$ is identical under both failure scenarios indicated by (25) and (26). Therefore, we can further conclude from (61) that λ_{A_1} , i.e. the stability property of internal dynamics, remain invariant despite the failure type if $|\chi|$ is fixed.

C. Case Study: Selection of $|\chi|$

As previous analysis presents, parameter $|\chi|$ need to be selected such that : (1) The matrix A_1 in (50) is Hurwitz for stable internal dynamics. (2) Condition (40) is satisfied for an acceptable control effectiveness on y_2 .

In this section, we conduct a case study on a specific type of quadrotor, a modified Parrot Bebop2, in the simulation to demonstrate the effect of $|\chi|$ on the overall controller performance. The inertial and geometric property of this quadrotor is listed in Table III. Without loss of generality, we assume rotor 2 and 4 are removed ($s_n = -1, s_l = 1, \chi = |\chi|$). Thus from (60), we have $\bar{r} = 26.4$ rad/s, $\bar{\omega} = 1015$ rad/s.

The top plot in Fig. 5 shows the poles of A_1 versus $|\chi| \in (\zeta, \zeta + \pi)$. Note that $|\chi| = \zeta + k\pi$ ($k \in \mathbb{Z}$) causes singularity as (50) shows. The shaded gray area represents positive real part

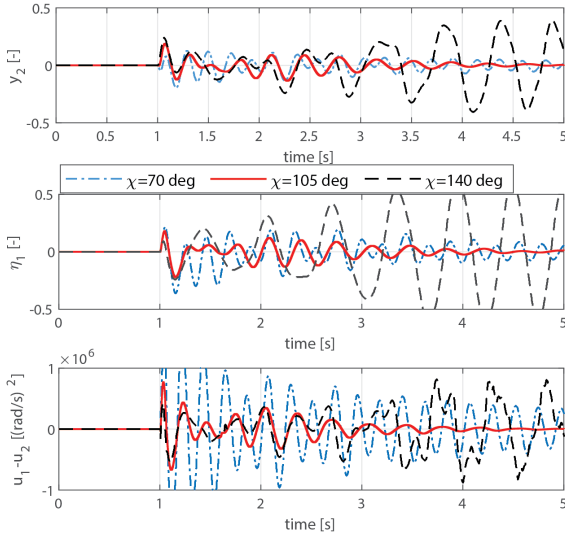


Fig. 6: Time series of y_2 , η_1 , and $u_1 - u_2$ of three tests with different $|\chi|$ in the simulation. A step-input of position command is given at $t = 1$ s.

of poles that render unstable internal dynamics. The bottom plot in Fig. 5 presents $r_B(|\chi|)$ as given in (40) with different $|\chi|$. The shaded red represents the violation of the constraint $r_B \geq 1$.

In the simulation, the quadrotor is commanded to transfer from $X = 0$ to $X = 3$ m at $t = 1$ s. Various selections of $|\chi|$ are tested and given in the bottom plot of Fig. 5. The flights within the unshaded area succeed in conducting the transfer maneuver, whereas most of those in the shaded area failed.

Three tests in the simulation with respective $|\chi|$ equal to 70, 105, and 140 degrees are further demonstrated. Fig. 6 shows the time series of output y_2 , internal state η_1 , and $u_1 - u_2$ of these three flights. When $|\chi| = 105$ deg, the transition is successful where both y_2 and internal states η_1 converge to zero. As $|\chi| = 70$ deg, the violation of constraint $r_B \leq 1$ leads to a small control effectiveness \hat{B}_2 . As a result, $u_1 - u_2$ significantly oscillates during the maneuver and the drone crashed due to limited actuator dynamics. On the other hand, when $|\chi| = 140$ deg, the internal dynamics are unstable and divergent oscillation of η_1 occurs that makes the drone crash.

VI. GENERALIZATION TO OTHER FAILURE CONDITIONS

In this section, the inner-loop control scheme introduced in Sec. IV is generalized to a quadrotor with complete loss of a single rotor, or without rotor failure (nominal condition).

A. Single Rotor Failure

1) *Internal Dynamics Analysis:* For a quadrotor with a single rotor failure, there are three permitted inputs. Therefore, three outputs can be defined. Similar to the double-rotor-failure condition, one output is defined as the altitude:

$$y_1 = Z \quad (62)$$

The other two outputs are related to the reduced attitude control:

$$y_2 = h_1 - n_x^B \quad (63)$$

$$y_3 = h_2 - n_y^B \quad (64)$$

To align the body fixed unit vector $\mathbf{n}^B = [n_x^B, n_y^B, n_z^B]^T$ with the reference $\mathbf{n}_d^B = [h_1, h_2, h_3]^T$, the preceding y_2 and y_3 should be stabilized to zero.

The relative degrees of the inner-loop system are $\rho_1 = \rho_2 = \rho_3 = 2$ from (27). Therefore, the external states are

$$\begin{bmatrix} \xi_1 \\ \xi_2 \\ \xi_3 \\ \xi_4 \\ \xi_5 \\ \xi_6 \end{bmatrix} = \begin{bmatrix} y_1 \\ \dot{y}_1 \\ y_2 \\ \dot{y}_2 \\ y_3 \\ \dot{y}_3 \end{bmatrix} = \begin{bmatrix} Z \\ V_z \\ h_1 - n_x^B \\ -h_3q + h_2r \\ h_2 - n_y^B \\ h_3p - h_1r \end{bmatrix} \quad (65)$$

Note that $\mathbf{x}_{in} \in \mathbb{R}^7$ and there are 6 external states, the only internal state can be selected as

$$\eta_1 = r + \mu_1 V_z + \mu_2 p + \mu_3 q \quad (66)$$

where μ_1, μ_2, μ_3 are calculated such that $\dot{\eta}_1$ does not include the control input. These coefficients are constant and related to the handedness of the remaining rotors.

After some tedious algebra, the zero dynamics can be calculated as

$$\dot{\eta}_1 = -\frac{\gamma}{\Theta} \eta_1 + \frac{\Pi}{h_3 \Theta^2} \eta_1^2 + g \mu_1 \quad (67)$$

where

$$\Theta = n_x^B \mu_2 / h_3 + n_y^B \mu_3 / h_3 + 1 \quad (68)$$

$$\Pi = A_z n_x^B n_y^B / h_3 + A_x n_y^B \mu_2 + A_y n_x^B \mu_3 \quad (69)$$

Particularly, when $n_x^B = n_y^B = 0$, namely the drone spins about its thrust direction, we have

$$\dot{\eta}_1 = -\gamma(\eta_1 - \bar{\eta}_1) \quad (70)$$

Since the yaw damping $\gamma > 0$, the internal state η_1 at the equilibrium $\bar{\eta}_1$ is stable.

2) *Control Law:* The above analysis demonstrates that the stability of internal dynamics with the selection of outputs in (62)-(64). After selecting the control outputs, the same control scheme presented in Fig. 2 can be applied for the single rotor failure condition. Without loss of generality, we assume that rotor 4 is removed, then we have

$$\mathbf{u} = [\omega_1^2, \omega_2^2, \omega_3^2]^T \quad (71)$$

With the same procedure introduced in Sec. IV, the control law for a quadrotor subjected to a single rotor failure can be obtained using (22), where

$$\mathbf{v} = \begin{bmatrix} -k_{z,p}(\xi_1 - Z_{\text{ref}}) - k_{z,d}(\xi_2 - \dot{Z}_{\text{ref}}) + \ddot{Z}_{\text{ref}} \\ -k_{a,p}\xi_3 - k_{a,d}\xi_4 \\ -k_{a,p}\xi_5 - k_{a,d}\xi_6 \end{bmatrix} \quad (72)$$

$$\ddot{\mathbf{y}}_f = [\dot{a}_{z,f}/R_{33,f}, \ddot{h}_{1,f}, \ddot{h}_{2,f}]^T \quad (73)$$

The control effectiveness matrix $\hat{\mathbf{B}}$ can be estimated using (5) and (6):

$$\hat{\mathbf{B}}(\mathbf{x}_f) = \begin{bmatrix} -\bar{k}R_{33,f}/m_v & -\bar{k}R_{33,f}/m_v & -\bar{k}R_{33,f}/m_v \\ -\bar{k}b\sin\beta & \bar{k}b\sin\beta & \bar{k}b\sin\beta \\ \bar{k}b\cos\beta & \bar{k}b\cos\beta & -\bar{k}b\cos\beta \end{bmatrix} \quad (74)$$

TABLE I: Parameters of the tested quadrotor.

par.	value	unit	par.	value	unit
I_x	$1.45e^{-3}$	$\text{kg} \cdot \text{m}^2$	m_v	0.410	kg
I_y	$1.26e^{-3}$	$\text{kg} \cdot \text{m}^2$	b	0.145	m
I_z	$2.52e^{-3}$	$\text{kg} \cdot \text{m}^2$	β	52.6	deg
I_p	$8.00e^{-6}$	$\text{kg} \cdot \text{m}^2$	γ	$1.50e^{-3}$	$\text{N} \cdot \text{m} \cdot \text{s}$
$\bar{\kappa}$	$1.90e^{-6}$	$\text{kg} \cdot \text{m}^2$	σ	0.01	m

B. Without Rotor Failure

For a multi-rotor drone with more than three actuators, such as a nominal quadrotor or a hexacopter, there are four or more permitted control inputs. We can then introduce the fourth output related to the yaw control:

$$y_4 = r \quad (75)$$

An independent yaw controller can be appended to provide the reference yaw rate r_{ref} , such as a PD controller:

$$r_{\text{ref}} = -k_{p,\psi} e_\psi - k_{d,\psi} \dot{e}_\psi \quad (76)$$

where e_ψ is the yaw angle tracking error; $k_{p,\psi}$ and $k_{d,\psi}$ are positive gains.

In this case, the number of control input is equal or greater than the output. Then the control effective matrix $\hat{\mathcal{B}}(\mathbf{x}_f)$ has full column rank. We can obtain the control law as

$$\mathbf{u}_{\text{indi}} = \hat{\mathcal{B}}(\mathbf{x}_f)^+ (\mathbf{v} - \ddot{\mathbf{y}}_f) + \mathbf{u}_f \quad (77)$$

where superscript $[\cdot]^+$ indicates the Moore-Penrose inverse of the matrix. Note that the rotor angular acceleration $\dot{\omega}_i$ may deteriorate the yaw control performance while implementing this approach. Interested readers are referred to [21] to tackle this problem for a nominal quadrotor.

VII. EXPERIMENTAL VALIDATION

The proposed control method has been validated on a modified Parrot Bebop2 drone with a lighter battery and camera module removed. The geometric and moment of inertia properties are given in Table III. During the flight test, a motion capturing system (OptiTrack) with 12 cameras provided the position measurements of the 4 markers attached to the drone at 120 Hz. The inertial measurement unit (IMU) measured the angular rates (from gyroscope) and the specific

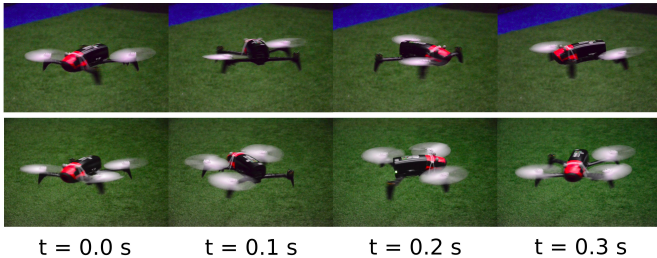


Fig. 7: Snapshot of the tested Bebop2 subjected to failures of rotor 1 & 3 (upper row), and subjected to failure of rotor 3 (bottom row).

TABLE II: Control gains.

outer	k_p [s^{-2}]	k_i [s^{-3}]	k_d [s^{-1}]	
-loop	1.0	0.1	1.0	
inner	$k_{a,p}$ [s^{-2}]	$k_{a,d}$ [s^{-1}]	$k_{z,p}$ [s^{-2}]	$k_{z,d}$ [s^{-1}]
-loop	50	30	15	10

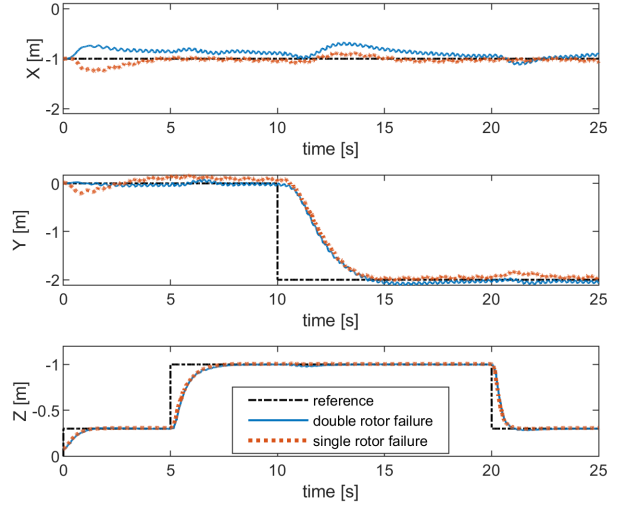


Fig. 8: Position tracking task under windless condition. The double-rotor-failure condition (blue solid line) and single rotor failure condition (red dash line) to track the reference position (black dot dash line).

force (from the accelerometer) at 512 Hz. A built-in brushless DC (BLDC) motor controller controlled the rotor speeds of each propeller, and also measured the rotor rotational rates in RPM at 512 Hz. Subsequently, an Extended Kalman Filter (EKF) was implemented to estimate the position, velocity of the center of mass, and the attitude of the body frame. The proposed controller and the EKF were run onboard at 500 Hz with the original processor Parrot P7 dual-core CPU Cortex 9. The control gains are given in Table II.

A. Flights with Double and Single Rotor Failure

The first set of flights tested the 3-D trajectory tracking of the quadrotor without wind disturbance. Fig. 7 presents snapshots of the tested quadrotor with double/single rotor failure within 0.3 s. In Fig. 8, the reference position together with the measured position of the quadrotor with double/single rotor failure are given.

Without loss of generality, we removed the rotor 1 and rotor 3 for the double rotor failure case. Fig. 9a shows the second output y_2 and the first internal state η_1 . As is introduced in Sec. IV, they represent the reduced attitude and need to converge to zero. Despite the misalignment during the take-off maneuver at the first 3 seconds, a slight tracking error of y_2 is observed which is presumably due to the bias of the center of mass. In this flight, $|\chi| = 90$ deg was selected for stable internal dynamics. Consequently, the internal state η_1

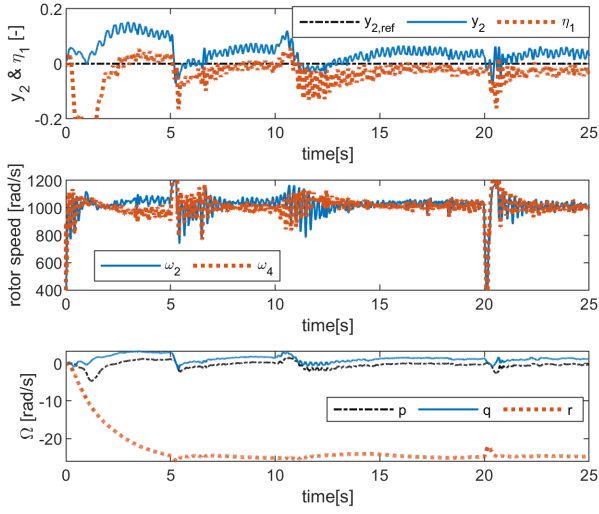


Fig. 9: Variables during the position tracking flight test with failures of rotor 1 and rotor 3. From top to bottom are: the output y_2 and internal state η_1 ; the angular speed measurements of the rotor 2 and rotor 4; the angular rates measurements.

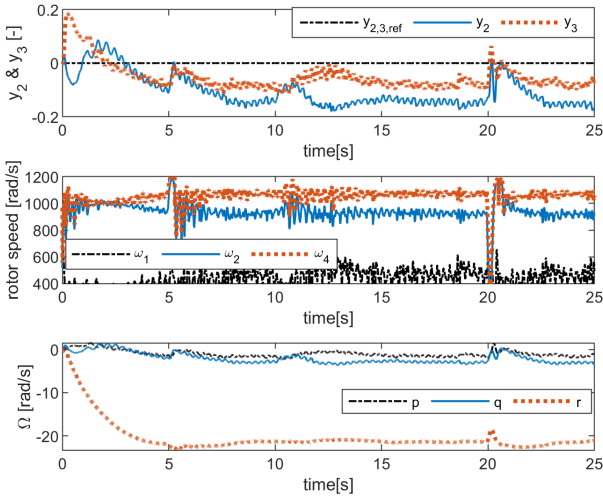


Fig. 10: Variables during the position tracking flight test with failure of rotor 3. From top to bottom are: the output y_2 and y_3 ; the angular speed measurements of the rotor 1, 2, and 4; the angular rates measurements.

was confined around zero. Fig. 9b shows the angular speeds of rotor 2 and 4 that remained almost constant at $\bar{\omega} = 1000$ rad/s during the horizontal maneuvers, which was in-line with the *Assumption 3*. A yaw rate at about -25 rad/s shown in Fig. 9c indicates the fast spinning motion of the damaged quadrotor.

With the same controller and the same set of gains, the condition with single rotor failure was also tested. The rotor 3 was removed in this test. As is shown in Fig. 10a, the internal state η_1 is replaced by the third output y_3 because of the addition of one rotor compared to the double-rotor-failure

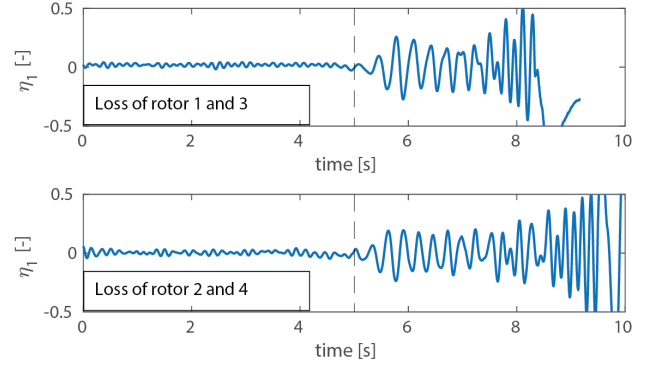


Fig. 11: Internal state η_1 in with different selection of $|\chi|$. Before $t = 5$ s, $|\chi| = 90$ deg is selected which leads to stable internal dynamics in both conditions. After $t = 5$ s, $|\chi|$ is changed to 180 deg and the internal dynamics become unstable.

condition. The reference $y_{2,\text{ref}} = y_{3,\text{ref}} = 0$ was employed in this flight that required the rotor 1 (the one diagonal to the failed rotor) to generate no force. However, due to the lower saturation of rotor 1 presented in Fig. 10b, a constant tracking error of y_2 and y_3 are observed. In spite of these attitude tracking errors, the drone under both single/double rotor failure cases were able to track the position commands.

B. Effect of χ in the Double-Rotor-Failure Condition

The quadrotor in the double-rotor-failure condition was tested in the hover region with different sets of $|\chi|$ to experimentally demonstrate its effect on the stability of the internal dynamics. Fig. 11 shows the internal state η_1 during a hovering flight where the parameter $|\chi|$ was initialized at 90 deg which would lead to stable internal dynamics. At $t = 5$ s, $|\chi|$ was changed to 180 deg during the flight and the internal state became unstable. This complies with the prediction from *Proposition 1*.

It is noteworthy that the stable region boundary moves slightly to the right compared to the theoretical prediction, as is shown in Fig. 5. As a consequence, the admissible region of $|\chi|$ becomes larger. The difference might come from the omission of the aerodynamic damping on pitch and roll rate while conducting internal dynamic analysis.

VIII. VALIDATIONS IN A WIND TUNNEL

To validate the robustness against unmodeled aerodynamic forces and moments in the high-speed flight regime, flight tests have been carried out in the Open Jet Facility (OJF), a large scale wind tunnel with an aperture of 2.85 meters (see Fig. 12). The parameter $|\chi| = 105$ deg that lies roughly in the center of its admissible region is selected, as Fig. 5 illustrates.

The linear quadratic regulator (LQR) is selected as the baseline for comparison in the wind tunnel. This method has been validated in practice in a milestone research paper [14]. The same set of gains from this paper were implemented for comparison. Specifically, the cost on control inputs was set to

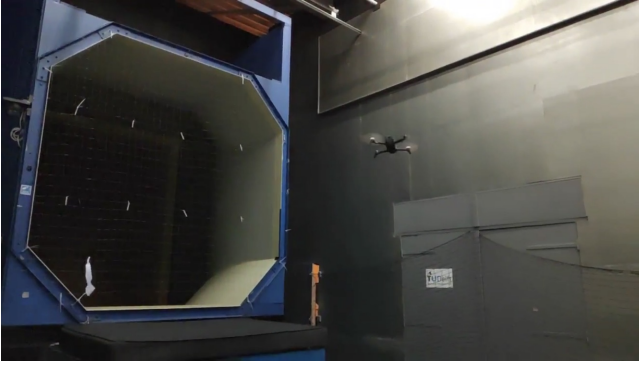


Fig. 12: Snapshot of the tested quadrotor in the wind tunnel, with removal of rotor 1 and 3.

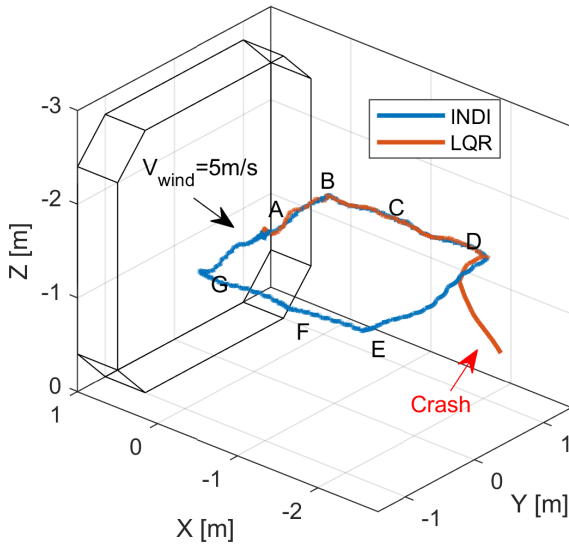


Fig. 13: 3D trajectories of the damaged quadrotor under $V_{\text{wind}} = 5$ m/s, where A to G represent the setpoints. INDI finished the trajectory tracking task while LQR failed during the transition from setpoint D to E.

one; the cost on the reduced attitude was set to 20 and the cost on angular rates was set to zero. Since a different drone was used, the time constant of the first-order actuator model is set as 30 ms that differs from the literature. Both INDI and LQR used the same outer-loop control gains as given in Table. II.

A. Trajectory Tracking Task

A trajectory tracking task was performed under a wind flow of 5 m/s. The wind flow was along the negative direction of the x_I axis. Fig. 13 plots the trajectories using INDI and LQR respectively. The drone tracked setpoints A to G in sequence every 3 seconds. In addition, the step reference positions (X_{ref} and Y_{ref}) were smoothed by a first-order filter with a time constant 1 s. As Fig. 13 shows, both methods successfully tracked the setpoints before point D. However, the LQR approach failed during the transition from setpoint D to E, which was perpendicular to the wind flow.

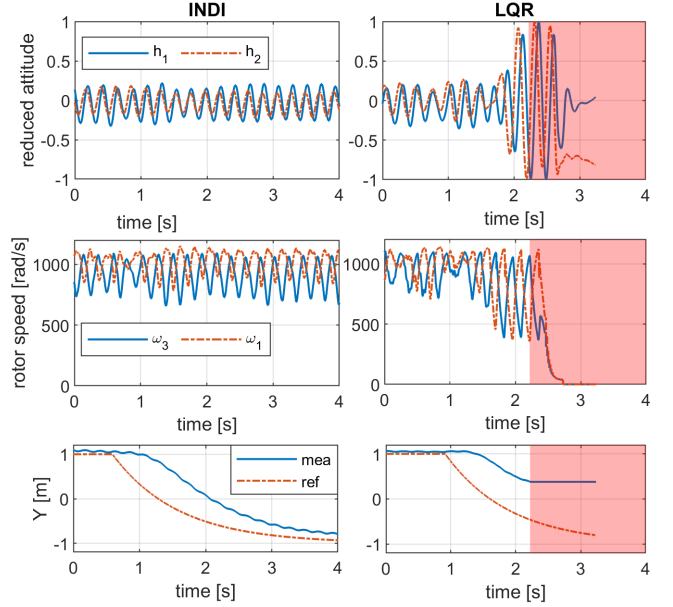


Fig. 14: Reduced attitude, rotor speeds and lateral position Y of the quadrotor during the transition from setpoint D to E. The reduced attitude of the drone controlled by LQR became unstable, before the loss of OptiTrack measurement shaded in red, and eventually crashed. In comparison, the drone controlled by the INDI approach succeeded to finish this maneuver.

TABLE III: Maximum flight speed of the INDI and LQR controller with various control gains. Q for LQR indicates the cost on the reduced attitude.

INDI			LQR	
$k_{a,p}$	$k_{a,d}$	V_{max} [m/s]	Q	V_{max} [m/s]
5	1	7.8	1	4.6
10	2	8.3	3	5.9
50*	30*	8.8	10	5.2
100	30	8.2	20*	5.1
200	50	7.8	30	6.3

*Gains for the trajectory tracking task.

Fig. 14 compares states between the two approaches in this period. From the plotted data, we can find that the reduced attitudes of both methods were bounded before conducting the maneuver, despite oscillations of reduced attitude and rotor speeds caused by the wind flow and yaw motion. During the maneuver from point D to E, the reduced attitude of the LQR approach diverged from zero (the linearization point). The instability of the inner-loop attitude control caused the failure of trajectory tracking and eventually lead to a crash.

For LQR, the rotor speed commands (i.e. the control input) were naturally amplified (at around $t = 2$ s in the mid-right plot of Fig. 14) to stabilize the reduced attitudes (h_1 and h_2) as they were diverging from the equilibrium (top-right plot). These increase of control input may destabilize the system in

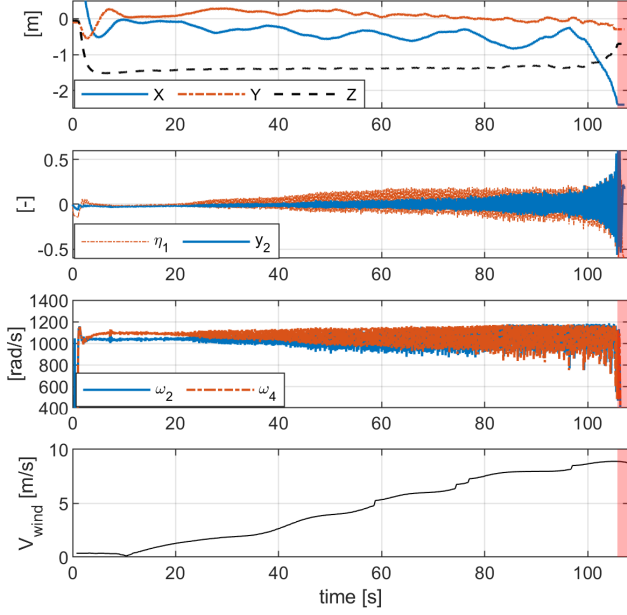


Fig. 15: Variables during the wind-tunnel maximum flight speed test of INDI. From top to bottom are: positions of the drone; the internal state η_1 and the output y_2 ; the angular speed of the remaining rotor (rotor 2 & 4); the time series of the wind speed which gradually increased until the loss-of-control happened. The red area represents loss of OptiTrack measurement.

the presence of nonlinearities and model uncertainties caused by the wind flow. By contrast, the INDI approach used the second-order derivative of the reduced attitude ($y_f^{(p)}$ in (22)) to compensate for the model uncertainties. The nonlinearities are also handled by the feedback linearization step of INDI. Thereby the reduced attitude can be stabilized without drastically increasing the control input.

B. Maximum Flight Speed Test

To explore the maximum flight speed of a quadrotor under the failure of two opposing rotors, maximum speed flight tests were conducted using both INDI and LQR. During the entire flight, the drone was hovering at a setpoint located in front of the wind tunnel ($\mathbf{P}_{\text{ref}} = [0, 0, -1.5]^T$). The wind speed was gradually increased from $V_{\text{wind}} = 0$ to a V_{max} until the drone crashed.

Table. III compares the maximum flight speed achieved by the two approaches with different set of gains. Similarly to the trajectory tracking task in the preceding section, INDI outperforms the LQR approach in terms of maximum flight speed. Be that as it may, the drone controlled by LQR was still stabilized at relatively high-speeds thanks to the inherent stabilizing property of feedback control.

Fig. 15 shows the time series of position, η_1 , y_2 , rotor speeds and wind speed during a flight controlled by INDI, where the drone crashed at $V_{\text{wind}} = 8.8$ m/s when $t = 107$ s. The variations of η_1 , y_2 and rotor speeds significantly increased with the

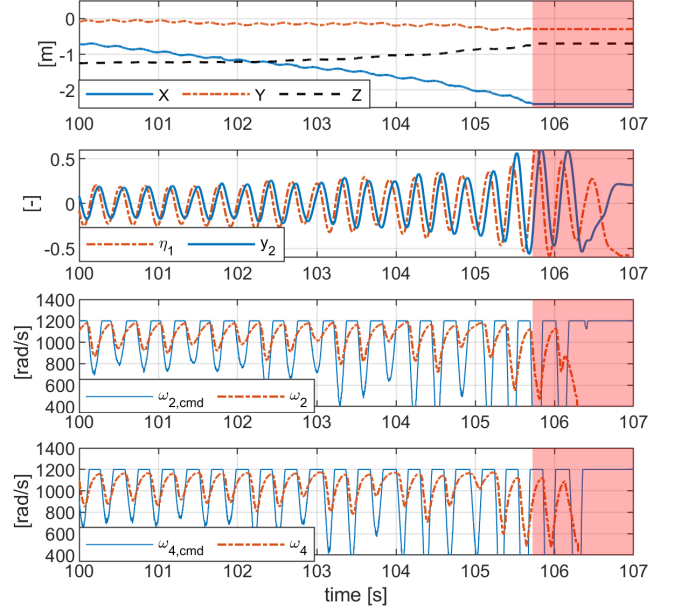


Fig. 16: Close-up of the variables of Fig. 15 during last 7 seconds before the crash. The red area represents loss of OptiTrack measurement.

wind speed. Despite the gradual increase of the oscillation, the internal state η_1 was bounded near zero and subsequently ensured successful position tracking.

To investigate the cause of loss-of-control of INDI, Fig. 16 shows the close-up of Fig. 15 during the last 7 seconds before the crash. In addition to the rotor speed measurements, the rotor speed commands are also plotted. From the reduction of X in the top plot, we can find that the quadrotor was blown away from the setpoint along the wind flow. Meanwhile, the increase of Z indicates the continues reduction of the altitude in this process. These phenomena are believed caused by the saturation of motors under wind resistance, which can be clearly seen in the bottom two plots of Fig. 16. In addition to the motor saturation, the control input lag due to motor dynamics can be observed, which may cause the gradual divergence of η_1 and y_2 in the second plot of Fig. 16. We hence infer that the motor capacity (bandwidth and power limit) is a major limiting factor of the maximum flight speed.

C. High-Speed Flight with Imperfect State Estimations

Since the ultimate goal of this work is improving drone safety during the high-speed flight in outdoor environments, preliminary validations of the proposed method using imperfect state estimations have been conducted in the wind-tunnel. The sampling rate of the motion capturing system was reduced from 120 Hz to 10 Hz to simulate GPS-like update rates. Only position measurements were transmitted to the onboard flight controller. A complementary filter [35] was implemented by fusing the measurements from the IMU and the magnetometer, to provide attitude estimates.

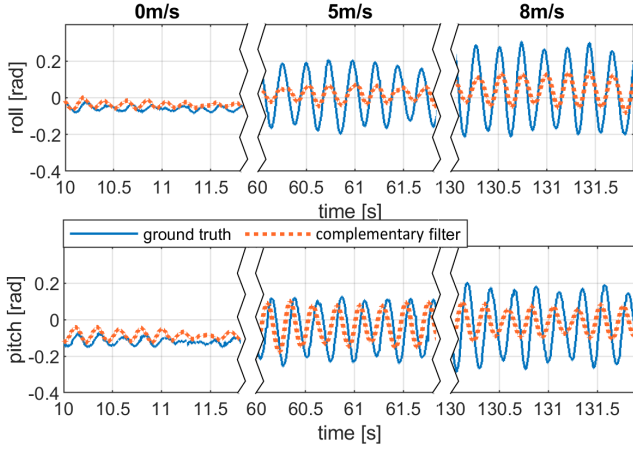


Fig. 17: Comparison of pitch and roll estimations between the complementary filter and the ground truth in different flight speeds demonstrating degradation of the compensatory filter at these condition.

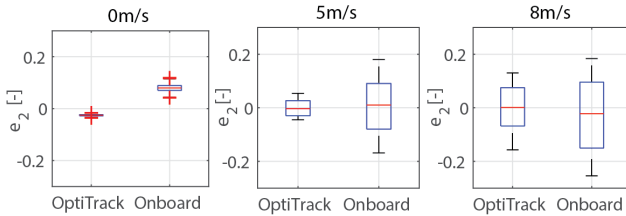


Fig. 18: Boxplots comparing the tracking error of y_2 , denoted by e_2 , between flights with OptiTrack aided attitude estimation and those with onboard complementary filter, in different flight speeds.

In this setting, the INDI controlled drone achieved controlled flight at 8.4 m/s inside the wind tunnel, indicating robustness to significant attitude estimation errors. These errors can be seen in Fig. 17, which compares the pitch and roll angles from the onboard complementary filter with the ground truth obtained with the OptiTrack system at three different flight speeds. As a consequence, the tracking errors of the reduced attitude were greater using the onboard complementary filter, especially at 0m/s and 5m/s as Fig. 18 shows. Note that the increase of tracking error was less apparent at 8m/s where the drone was near the flight envelope boundary, because the controller performance was not only degraded by imperfect state estimations, but also motor limitations.

We hypothesize that the degradation of the complementary filter is caused by the strong aerodynamic forces and centrifugal forces measured by the accelerometers. Improving the accuracy of the state estimator at high flight speeds and high angular rate conditions is out of the scope of this paper, but it is a highly recommended future research.

IX. CONCLUSION

In this research, an incremental nonlinear fault-tolerant control method is developed for a quadrotor subjected to complete loss of two opposing rotors. The internal dynamics

of this under-actuated control problem is analyzed. Thereby a criterion is given to select proper control outputs that guarantee the stability of internal dynamics, which has been validated in both simulations and flight tests. The control scheme can be generalized to a nominal quadrotor, or one with the loss of a single rotor.

The proposed method uses the incremental nonlinear dynamic inversion (INDI) approach to control the selected outputs. The INDI approach replaces non-input related model terms with sensor measurements, which reduces the model dependencies and consequently increases the robustness against wind disturbances in the high-speed flight regime. Flight tests of a quadrotor with complete loss of two opposing rotors are conducted in an open jet wind tunnel. In the presence of significant aerodynamic effects, the control method is able to stabilize the quadrotor at over 8.0 m/s. Compared with the linear quadratic regulator (LQR) approach, the proposed method was found to have better robustness against model uncertainties brought by the significant aerodynamic effects.

Flights with imperfect state estimations from onboard sensors have been conducted. Flight data in the high-speed regime with onboard sensors reveal the adverse effects of aerodynamics on the state estimation. Future work is recommended to focus on improving the attitude estimation using onboard sensors by taking into account the effect of aerodynamics and high angular rate motion on the state estimator.

ACKNOWLEDGMENT

The authors would like to thank the help from Leon Sijbers, Bram Strack van Schijndel, and the support from MAVLab, Open Jet Facility of Delft University of Technology.

REFERENCES

- [1] T. Li, Y. Zhang, and B. W. Gordon, "Passive and active nonlinear fault-tolerant control of a quadrotor unmanned aerial vehicle based on the sliding mode control technique," *Special Issue Article Proc IMechE Part I: J Systems and Control Engineering*, vol. 227, no. 1, pp. 12–23, 2012.
- [2] L. Besnard, Y. B. Shtessel, and B. Landrum, "Quadrotor vehicle control via sliding mode controller driven by sliding mode disturbance observer," *Journal of the Franklin Institute*, vol. 349, no. 2, pp. 658–684, 2012.
- [3] X. Wang, S. Sun, E.-J. van Kampen, and Q. Chu, "Quadrotor Fault Tolerant Incremental Sliding Mode Control driven by Sliding Mode Disturbance Observers," *Aerospace Science and Technology*, vol. 87, pp. 417–430, 2019.
- [4] X. Wang, E. J. van Kampen, and Q. Chu, "Quadrotor fault-tolerant incremental nonsingular terminal sliding mode control," *Aerospace Science and Technology*, 2019.
- [5] A. Lanzon, A. Freddi, and S. Longhi, "Flight Control of a Quadrotor Vehicle Subsequent to a Rotor Failure," *Journal of Guidance, Control, and Dynamics*, vol. 37, pp. 580–591, 3 2014.
- [6] V. Lippiello, F. Ruggiero, and D. Serra, "Emergency landing for a quadrotor in case of a propeller failure: A backstepping approach," in *IEEE International Conference on Intelligent Robots and Systems*, no. Iros, pp. 4782–4788, 2014.
- [7] V. Lippiello, F. Ruggiero, and D. Serra, "Emergency landing for a quadrotor in case of a propeller failure: A PID Based Approach," in *IEEE International Conference on Intelligent Robots and Systems*, pp. 4782–4788, 2014.
- [8] P. Lu and E.-j. V. Kampen, "Active fault-tolerant control for quadrotors subjected to a complete rotor failure," pp. 4698–4703, 2015.
- [9] Y. V. Morozov, "Emergency Control of a Quadcopter in Case of Failure of Two Symmetric Propellers," *Automation and Remote Control*, vol. 79, no. 3, pp. 463–478, 2018.
- [10] D. Crousaz, F. Farshidian, M. Neunert, and J. Buchli, "Unified Motion Control for Dynamic Quadrotor Maneuvers Demonstrated on Slung Load and Rotor Failure Tasks," pp. 2223–2229, 2015.

- [11] M. W. Mueller and R. D'Andrea, "Stability and control of a quadcopter despite the complete loss of one, two, or three propellers," *Proceedings - IEEE International Conference on Robotics and Automation*, pp. 45–52, 2014.
- [12] A.-r. Merheb and H. Noura, "Emergency Control of AR Drone Quadrotor UAV Suffering a Total Loss of One Rotor," vol. 22, no. 2, pp. 961–971, 2017.
- [13] J. Stephan, L. Schmitt, and W. Fichter, "Linear Parameter-Varying Control for Quadrotors in Case of Complete Actuator Loss," *Journal of Guidance, Control, and Dynamics*, vol. 41, no. 10, pp. 2232–2246, 2018.
- [14] M. W. Mueller and R. D'Andrea, "Relaxed hover solutions for multicopters: Application to algorithmic redundancy and novel vehicles," *The International Journal of Robotics Research*, p. 0278364915596233, 2015.
- [15] W. Zhang, M. W. Mueller, and R. D'Andrea, "A controllable flying vehicle with a single moving part," *Proceedings - IEEE International Conference on Robotics and Automation*, vol. 2016-June, pp. 3275–3281, 2016.
- [16] C. Russell, J. Jung, G. Willink, and B. Glasner, "Wind tunnel and hover performance test results for multicopter UAS vehicles," *Annual Forum Proceedings - AHS International*, 2016.
- [17] S. Sun, C. C. de Visser, and Q. Chu, "Quadrotor Gray-Box Model Identification from High-Speed Flight Data," *Journal of Aircraft*, pp. 1–17, 11 2018.
- [18] S. Sieberling, Q. P. Chu, and J. a. Mulder, "Robust Flight Control Using Incremental Nonlinear Dynamic Inversion and Angular Acceleration Prediction," *Journal of Guidance, Control, and Dynamics*, vol. 33, no. 6, pp. 1732–1742, 2010.
- [19] P. Acquatella, W. Falkena, E. van Kampen, and Q. P. Chu, "Robust Nonlinear Spacecraft Attitude Control using Incremental Nonlinear Dynamic Inversion," *AIAA Guidance, Navigation, and Control Conference*, no. August, pp. 1–20, 2012.
- [20] P. Simplício, M. D. Pavel, E. van Kampen, and Q. P. Chu, "An acceleration measurements-based approach for helicopter nonlinear flight control using incremental nonlinear dynamic inversion," *Control Engineering Practice*, vol. 21, no. 8, pp. 1065–1077, 2013.
- [21] E. J. J. Smeur, Q. Chu, and Guido C. H. E. de Croon, "Adaptive Incremental Nonlinear Dynamic Inversion for Attitude Control of Micro Aerial Vehicles," *Journal of Guidance, Control, and Dynamics*, vol. 39, no. 3, pp. 450–461, 2016.
- [22] E. J. Smeur, G. C. De Croon, and Q. Chu, "Gust Disturbance Alleviation with Incremental Nonlinear Dynamic Inversion," in *IEEE International Conference on Intelligent Robots and Systems*, vol. 2016-Novem, pp. 5626–5631, 2016.
- [23] E. Tal and S. Karaman, "Accurate Tracking of Aggressive Quadrotor Trajectories Using Incremental Nonlinear Dynamic Inversion and Differential Flatness," *Proceedings of the IEEE Conference on Decision and Control*, vol. 2018-December, no. Cdc, pp. 4282–4288, 2019.
- [24] S. Sun, L. Sijbers, X. Wang, and C. de Visser, "High-Speed Flight of Quadrotor Despite Loss of Single Rotor," *IEEE Robotics and Automation Letters*, vol. 3, pp. 3201–3207, 10 2018.
- [25] X. Yun and Y. Yamamoto, "Internal dynamics of a wheeled mobile robot," in *Proceedings of 1993 IEEE/RSJ International Conference on Intelligent Robots and Systems (IROS '93)*, vol. 2, pp. 1288–1294, IEEE, 1993.
- [26] F. Lewis, A. Das, and K. Subbarao, "Dynamic inversion with zero-dynamics stabilisation for quadrotor control," *IET Control Theory & Applications*, vol. 3, pp. 303–314, 3 2009.
- [27] E. M. Wallner and K. H. Well, "Attitude Control of a Reentry Vehicle with Internal Dynamics," *Journal of Guidance, Control, and Dynamics*, vol. 26, no. 6, pp. 846–854, 2003.
- [28] G. M. Hoffmann, H. Huang, S. L. Waslander, and C. J. Tomlin, "Precision flight control for a multi-vehicle quadrotor helicopter testbed," *Control Engineering Practice*, vol. 19, pp. 1023–1036, 9 2011.
- [29] R. Mahony, V. Kumar, and P. Corke, "Multirotor Aerial Vehicles: Modeling, Estimation, and Control of Quadrotor," *IEEE Robotics & Automation Magazine*, vol. 19, pp. 20–32, 9 2012.
- [30] S. Sun and C. de Visser, "Aerodynamic Model Identification of a Quadrotor Subjected to Rotor Failures in the High-Speed Flight Regime," *IEEE Robotics and Automation Letters*, vol. 4, pp. 3868–3875, oct 2019.
- [31] P. W. Fortescue and G. G. Swinerd, "Rigid-Body Attitude Control," *IEEE Control Systems*, vol. 31, pp. 30–51, 6 2011.
- [32] X. Wang, E.-J. Van Kampen, Q. P. Chu, and P. Lu, "Stability Analysis for Incremental Nonlinear Dynamic Inversion Control," in *2018 AIAA Guidance, Navigation, and Control Conference*, no. January, (Reston,

Virginia), pp. 1–16, American Institute of Aeronautics and Astronautics, 1 2018.

- [33] H. K. Khalil, “Nonlinear systems,” 2002.
- [34] X. Wang, E. J. Van Kampen, Q. Chu, and P. Lu, “Incremental sliding-mode fault-tolerant flight control,” *Journal of Guidance, Control, and Dynamics*, 2019.
- [35] R. Mahony, T. Hamel, and J. M. Pflimlin, “Nonlinear complementary filters on the special orthogonal group,” *IEEE Transactions on Automatic Control*, vol. 53, no. 5, pp. 1203–1218, 2008.